Case Studies in Thermal Engineering 42 (2023) 102751

Contents lists available at ScienceDirect

Case Studies in Thermal Engineering

journal homepage: www.elsevier.com/locate/csite

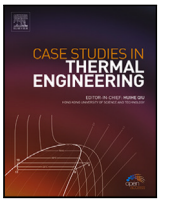

A numerical study of enhanced lithium-ion battery cooling using a module insert

Jeonggwan Han [a], Wonjin Ko [a], Myung-Seop Lim [a], Tonghun Lee [b], Jihyung Yoo [a,*]

[a] Department of Automotive Engineering (Automotive-Computer Convergence), Hanyang University, Seoul, 04763, South Korea
[b] Department of Mechanical Science and Engineering, University of Illinois at Urbana-Champaign, Urbana, IL, 61801, USA

ARTICLE INFO

Keywords:
Computational fluid dynamics
Lithium-ion battery
Conjugated heat transfer analysis
Heat generation modeling

ABSTRACT

Thermal performance of an electric vehicle (EV) battery module with an integrated cooling insert was numerically analyzed using computational fluid dynamics (CFD). Twelve NCM prismatic cells were packaged into a module where each cell was physically isolated from its neighboring cells by the cooling insert, designed to enhance the module's thermal performance. The battery cells and the cooling insert were attached to a thermal interface material (TIM) and a cooling plate with integrated liquid cooling where the coolant was a 50/50 ethylene glycol water (EGW) mixture. A heat generation model based on the discharge rate was used to assess the thermal responses of the module such as heat flux and temperature distribution. Thermal characteristics were studied under various discharge rates, coolant flow rates, insert thicknesses and material conditions. Results showed that the cooling insert reduced the cell temperature by 1.4 °C and increase the heat flux by 15.6% at 3 mm thickness with a coolant flow rate of 4 L/min. Cooling plates with plastic and metallic material properties were also studied and temperatures reductions up to 0.7 and 1.0 °C were observed, respectively. Furthermore, temperature uniformity was maintained to within 0.3 °C across all twelve cells at a coolant flow rate of 9 L/min. The results of this study could potentially lead to the development of a compact and low-cost intra-cell heat spreader in a battery module that can be readily implemented in production EVs.

1. Introduction

The automotive industry is undergoing a once in a century paradigm shift as increasing environmental regulations and public interest push many manufacturers from internal combustion engines and fossil fuels to electric motors and batteries [1,2]. As such, research into improving the performance and efficiency of electric powertrain and energy storage for automotive applications have significantly increased [3]. In particular, advanced battery technologies such as $LiFePO_4$ (LFP) and cobalt-based Li-ion batteries have significantly increased the energy storage capacities of battery electric vehicles (BEVs) [4]. LFP batteries have lower energy densities but have higher thermal tolerance compared to other Li-ion batteries, the latter of which is one of the reasons why they are widely used in Chinese BEVs. NMC Li-ion batteries, on the other hand, have higher energy densities [5] thereby enabling more efficient and longer range vehicles, but are more susceptible to heat compared to LFP batteries [6].

Despite many benefits, improved performance of any Li-ion batteries may be undermined if they are subject to less-than ideal operating conditions [7]. For example, battery chemistry can be very sensitive to temperature [8,9]. Lower than optimal temperatures reduce electrochemical reaction rates thereby decreasing battery capacity [10], whereas higher than optimal temperatures

* Corresponding author.
E-mail address: jihyungyoo@hanyang.ac.kr (J. Yoo).

https://doi.org/10.1016/j.csite.2023.102751
Received 25 November 2022; Received in revised form 10 January 2023; Accepted 15 January 2023
Available online 20 January 2023

Nomenclature

V	voltage [V]
V_o	open circuit voltage [V]
R	internal resistance [Ω]
$\triangle S$	entropy change [J K^{-1} mol^{-1}]
F	Faraday constant [s A mol^{-1}]
I	current [A]
T	temperature [K]
n	number of transferred electron
p	pressure [Pa]
$\dot{Q}$	heat generation [W]
t	time [s]
c_p	specific heat [J kg^{-1} K^{-1}]
Re	Reynolds number ($Re = \rho \cdot v \cdot D_h \cdot \mu^{-1}$)
D_h	hydraulic diameter [m]
h	convective heat transfer coefficient [W m^{-2} K^{-1}]
ρ	density [kg m^{-3}]
ν	kinematic viscosity [m^2 s^{-1}]
λ	heat transfer coefficient [W m^{-1} K^{-1}]
μ	viscosity [kg m^{-1} s^{-1}]
gen	heat generation
irr	irreversible heat generation
rev	reversible heat generation
EGW	ethylene glycol Water
TIM	thermal interface material
LIB	lithium-ion battery
BEV	battery electric vehicle
$BTMS$	battery thermal management system
CFD	computational fluid dynamics
EV	electric vehicle
LFP	Lithium Iron Phosphate
NMC	Nickel Manganese Cobalt
OCV	open-circuit voltage
PCM	phase change material
$PHEV$	plug-in hybrid electric vehicle
SOC	state of charge
SOH	state of health

may increase unwanted reaction rates which ultimately reduce battery life and may even induce thermal runaway [11]. Internal defects and high charge/discharge rates can further induce higher internal heat generation thereby exacerbating thermal runaway. Furthermore, temperature variations across multiple battery cells within a module or a pack can induce internal resistance and capacity variations, ultimately resulting in reduced performance and inaccurate assessment of state of charge (SOC) and state of health (SOH) [12,13]. As such, a proper control of cell temperature and heat dissipation through a battery thermal management system (BTMS) is critical to battery lifespan, performance, and efficiency optimization [14–18]. A BTMS is designed to regulate a safe and optimal operating temperature, between 25 and 40 °C, and minimize temperature variation, to within several °C, across all cells in the module or pack.

Various techniques for regulating automotive battery temperatures based on air cooling [19–21], liquid cooling [22–24] and phase change material (PCM) [25,26] are being actively studied. Most air cooling techniques use fans to induce air flow over the battery and remove excess thermal energy. The heat transfer coefficient of the induced forced convection will depend on various factors such as air flow rate and surface area. Wang et al. [27] studied the effect of 18,650 Li-ion battery cell arrangement structures and fan placements on air cooling performance. The aforementioned studies compared various cell arrangement and found that an axisymmetric module provided the best air cooling performance, a rectangular module was the most cost-effective, and a hexagonal module was the most space-efficient. Also, fans mounted above the battery module produced the most effective air cooling regardless of the battery module design. Mahamud et al. [28] studied a reciprocating air flow duct to reduce temperature variations of an air-cooled battery system. A 120 s periodic air flow reciprocation reduced the temperature variation by 4 °C (72%), and reduced the

maximum cell temperature by 1.5 °C. Saw et al. [29] improved the cooling of circular 38,120 LFP cells by developing a duct that wraps around the battery cells and taking advantage of the compression and expansion of the air flow in the duct. Also, steady state 3D temperature distribution of the battery cells under various air flow rates were calculated using conjugate heat transfer (CHT) [30]. Numerical results identified a correlation between the Nusselt and the Reynolds number. However, cell temperatures exceeded the safe operating limit at high discharge rates and the authors suggested the use of higher air flow rates or liquid cooling.

In general, liquid cooling is preferred at higher battery capacities or charge/discharge rates. Huo et al. [31] suggested that a battery module be sandwiched between two liquid-cooled plates. Various factors including the number of cooling channels embedded into each cooling plate, flow rate, flow direction, external temperature were analyzed to determine the optimal cooling configuration. Results showed that liquid cooling was effective only when the external temperature did not exceed 35 °C. Liquid cooling channel configuration and coolant developments are also being actively researched, both experimentally and numerically. Pandchal et al. [32] and Jin et al. [33] studied liquid cooling using mini-channels and ultra-thin minichannels, respectively. Jarrett et al. [34] optimized a serpentine-channel cooling plate in which 18 design parameters were analyzed to optimize for coolant pressure drop, average temperature and temperature uniformity. Yang et al. [35] determined that liquid metal cooling produced a lower cell temperature and improved thermal uniformity compared to water cooling given the same flow rate condition. This is due to the much higher thermal conductivity of the liquid metal compared to water. Sefidan et al. [36] submerged a cylindrical Li-ion cell in coolant imbued with aluminium oxide nanoparticles and determined the cooling performance. Other researchers [37–43] compared the thermal transport phenomena of various nanofluids with water

Lastly, phase change material (PCM) is another promising thermal management technique that is being actively researched. Thermal equilibrium analyses have shown that PCM is more effective compared to air and liquid cooling [44–46]. Among various PCMs that are being considered for automotive battery thermal management, paraffin is the most suitable. However, as with most PCMs it has a relatively low thermal conductivity [47] and PCMs are usually applied in conjunction with air or water cooling. Ling et al. [48] compared the PCM cooling performance with and without forced air cooling and determined the hybrid cooling system (PCM with air cooling) to be more effective and maintained the temperature to within safe operating limits. Sabbah et al. [49] studied a PCM and air cooling system for small Li-ion batteries in PHEVs under various conditions such as discharge rate, cell temperature, and external temperature. The cell temperature did not exceed 55 °C even at an external temperature and discharge rate of 45 °C and 6.67C, respectively, without additional power draw for the cooling system.

The aforementioned studies represent only a fraction of the overall automotive battery thermal management strategy research. In many cases, however, the focus is to maximize temperature reduction using advanced cooling methods which may not be feasible in production vehicle environment where spaces are very limited and cost is prohibitive. It is therefore critical that a compact and inexpensive battery module technique is developed that can be integrated into existing design with minimal modifications. However, such studies are difficult to find in literature and so this study proposes a module-level battery cooling system that has a very small footprint and can be readily integrated into a high energy density battery packs in production EVs. In this study, a battery module containing 12 prismatic $Li[Ni_{1/3}Co_{1/3}Mn_{1/3}]O_2$ Li-ion cells were analyzed under various flow rates, discharge rates, cooling insert dimensions and materials using CFD. The thermal responses of the module such as temperature and heat flux distribution across the module were used to evaluate the effectiveness of the integrated cooling insert.

2. Methods

2.1. Battery module model

Li-ion battery packs used in BEVs are mostly cell-module-pack structures where a group of battery cells are made into modules and a group of modules are made into battery packs. Most studies treat a battery module in a pack as an integral unit [50] and as such all thermal analyses in this study was performed at the module level. The module is made up of 12 cells, a cooling insert, a thin thermal interface material (TIM), and a cooling plate with integrated cooling jacket. The cooling insert is a guide structure with 12 slots, one for each cell, that is designed to enhance the thermal performance of the module. It is open at the top and the bottom so that cells can be easily removed and be in direct contact with the TIM. Once a cell has been placed in a slot it is physically isolated from its neighboring cells. Heat generated by the cell's side and bottom surfaces are conducted to the cooling plate through the cooling insert and the TIM, respectively. Convection through the U-shaped cooling jacket ultimately removed the heat from the module into its surroundings. The coolant is a 50/50 Ethylene Glycol Water (EGW) mixture, a common coolant in automotive applications. A 3D model of the module and the dimensions for the cooling plate are provided in Fig. 1.

2.2. Li-ion cell heat generation model

Twelve 37Ah prismatic lithium-ion battery cell were individually modeled for this study. The anode and cathode were graphite and NCM, respectively. The electrolyte was made up of lithium hexafluorophosphate. Detailed battery specifications [51] and thermodynamic properties [52] of the module components are provided in Table 1 and 2, respectively. Battery discharge rates are usually given by the C-rate and is based on $I_t = C/1\,\mathrm{h}$ as defined in the IEC61434 standard [29]. I_t represents the discharge current during one hour discharge and C is the nominal capacity of a battery cell. C-rate is a multiple of I_t, such that higher C-rate corresponds to higher discharge rate, and shorter operating time. Conversely, lower C-rates (1/5–1/10 is typical in highway driving) corresponds to lower discharge rate, and longer operating time.

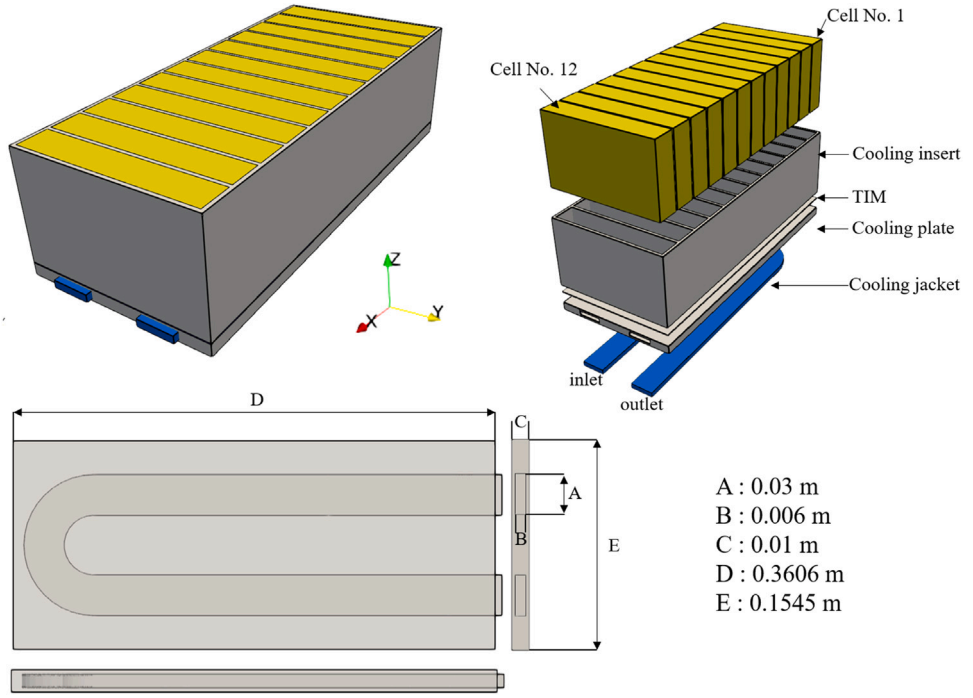

Fig. 1. Schematic and dimensions of the battery module and its components.

Table 1
Battery cell specifications.

Properties	Specification
Nominal capacity [Ah]	37
Nominal voltage [V]	3.7
Operating voltage [V]	2.8–4.2
Specific heat [J kg^{-1} K^{-1}]	1100
Thermal conductivity [W m^{-1} K^{-1}]	1.96:22.4:22.4
Size [mm]	91.6×148.5×26.8
Density [kg m^{-3}]	2630
Mass [kg]	0.82

Table 2
Thermodynamic properties of the battery module components and the coolant.

Property	Cooling insert & plate	TIM	Coolant
Thermal conductivity [W m^{-1} K^{-1}]	237	3	0.4108
Density [kg m^{-3}]	2702	2700	1050.44
Specific heat [J kg^{-1} K^{-1}]	903	1000	3499
Viscosity [kg m^{-1} s^{-1}]			1.538×10^{-3}

The two major sources of internal heat generation in a Li-ion battery cell are irreversible heat generation due to internal battery resistance and reversible heat generation due to entropy change [9]. Therefore, the total heat generated by each cell for a given C-rate can be calculated using models of internal resistance and entropy variations as a function of SOC as shown in Eq. (1),

$$\dot{Q}_{\text{gen}} = \dot{Q}_{\text{irr}} + \dot{Q}_{\text{rev}} = I(V_o - V) - IT\frac{dV_o}{dT} = I^2R - T \triangle S\frac{I}{nF}. \quad (1)$$

where V_o is the open circuit voltage (OCV), V is the cell voltage, R is the internal resistance of battery, $\triangle S$ is the changes of entropy, F is the Faraday constant (96485.4 C/mol). The model for internal resistance as a function of SOC can be found in Yang et al. [51]. The model for entropy change in an NCM-graphite lithium-ion battery can be found in Viswanathan et al. [53]. Overall, Eq. (1) can be represented as a function of SOC, wherein the SOC is expected to decrease linearly as a function of time at a given C-rate. Furthermore, since the current and voltage is a function of the SOC under constant C-rate, the above equation can be treated as a battery cell heat generation model as a function of time during discharge.

These models were used to perform transient analyses of 1C through 3C discharge cycles. The average heat generations at C-rates from 1C through 3C are provided in Table 3. These values were used to calculate the steady state temperature distribution and heat

Table 3
Average cell heat generation under various C-rates.

1C	2C	3C	4C	5C
1.95 W	7.06 W	15.33 W	26.76 W	41.35 W

flux under various C-rates, coolant flow rates, cooling insert materials and thicknesses. Transient analyses result under 1C and 2C discharge rates agreed very well with their respective steady-state results due to relatively mild heat generation. Transient results under 3C discharge rate showed slightly higher temperature discrepancy (up to 1°C in cell 8) compared to its steady-state solution. Due to minimal difference between the transient and steady-state results, all subsequent results have been calculated using the steady-state assumption.

2.3. Governing equations

Heat conduction in each battery cell, the cooling insert, the TIM, and the cooling plate as well as conduction and convection in the coolant were calculated using the following continuity, momentum, and energy equations [54]

$$\text{Continuity equation: } \frac{\partial \rho}{\partial t} + \frac{\partial u_i}{\partial x_i} = 0, \tag{2}$$

$$\text{Momentum equation: } \frac{\partial(\rho u)}{\partial t} + \frac{\partial(\rho u_i u_j)}{\partial x_j} = -\frac{\partial p}{\partial x_i} + \frac{\partial}{\partial x_j}(2\mu S_{ij} - \overline{\rho u_i' u_j'}), \tag{3}$$

$$\text{Energy equation: } \frac{\partial(\rho c_p T)}{\partial t} + \frac{\partial(\rho c_p u_j T)}{\partial x_j} = \frac{\partial}{\partial x_j}(\lambda \frac{\partial T}{\partial x_j} - \overline{\rho u_i' T'}) + Q_{gen}. \tag{4}$$

where u is velocity, ρ is density, p is pressure, Q_{gen} is heat generation, $S_{ij} = \frac{1}{2}(\frac{\partial u_i}{\partial x_j} + \frac{\partial u_j}{\partial x_i})$, ν is kinematic viscosity, λ is heat transfer coefficient, c_p is specific heat, $\overline{u_i' u_j'}$ is Reynolds stress, and $\overline{u_i' T'}$ is turbulent heat flux. The range of the Reynolds number in this study was between 630 and 7560. For turbulent flows, an improved two-equation eddy-viscosity turbulence model [55] and the hybrid wall model was used to calculate all layers near and far away from the wall for all flow conditions. Coefficients for the turbulence model can be found in [56].

$$\frac{\partial(\rho k)}{\partial t} + \frac{\partial(\rho u_j k)}{\partial x_j} = \tilde{P}_k - \beta^* \rho k \omega + \frac{\partial}{\partial x_j}\left[(\mu + \sigma_k \mu_t)\frac{\partial k}{\partial x_j}\right], \tag{5}$$

$$\frac{\partial(\rho \omega)}{\partial t} + \frac{\partial(\rho u_j \omega)}{\partial x_j} = \alpha \rho S^2 - \beta \rho \omega^2 + \frac{\partial}{\partial x_j}\left[(\mu + \sigma_\omega \mu_t)\frac{\partial \omega}{\partial x_j}\right] + 2(1 - F_1)\frac{\rho \sigma_{\omega 2}}{\omega}\frac{\partial k}{\partial x_j}\frac{\partial \omega}{\partial x_j}. \tag{6}$$

2.4. Numerical model: 3D model

Hexahedron mesh for each 3D models were created using the snappyhexmesh utility included in OpenFOAM. Finer mesh was applied near areas with high temperature gradients such as near boundaries and interfaces. Mesh independence was confirmed by comparing the maximum and minimum battery module temperatures using the same model under various mesh configuration from 3.1 to 26 million cells. Generally, numerical simulation is performed using an optimal number of mesh that provides a good balance of computational accuracy and cost. To that end, around 12 million meshes were used to model the temperature response of all 12 cells, cooling insert, TIM, cooling plate, and coolant in this study. The $y+$ value was kept under 1 and 10 for transition and turbulent flows at higher flow rates, respectively.

2.5. Numerical solver: OpenFOAM

Thermofluidic analyses of the battery module and its cooling system were conducted using OpenFOAM [57], a popular opensource CFD package with a worldwide user base. CFD is used to model a wide range of fluid flows and heat transfer applications [58,59]. A conjugate heat transfer solver (chtMultiRegionSimpleFoam in OpenFOAM 8) was used to calculate the 3D heat conduction in solids as well as conduction and convection in the coolant. The coolant inlet pressure gradient was set to a fixed value determined by the flow rate. The coolant outlet pressure was fixed at atmospheric pressure. The initial battery module and coolant temperatures were set to 25 °C. Exterior side walls of the cooling insert and the top of the module were cooled via natural convection ($h = 5\ W\ m^{-2}\ K^{-1}$). The averaged heat generation values (Table 3) were used for steady state analyze.

3. Results and discussions

Temperature distributions within the module were calculated under various cooling insert thicknesses and materials, C-rates, and coolant flow rate conditions to gauge the maximum and minimum cell temperatures as well as the module temperature uniformity. Furthermore, heat flux were also calculated to compare the thermal performance of various cooling insert properties.

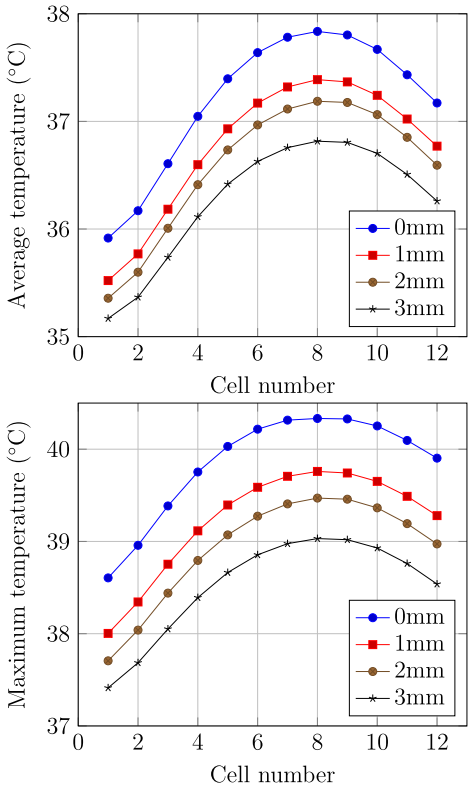

Fig. 2. (TOP) Average and (BOTTOM) maximum cell temperatures during 3C discharge rate and 4 L/min coolant flow rate.

Table 4
Average temperature data from Fig. 2.

	0 mm [°C]	1 mm [°C]	2 mm [°C]	3 mm [°C]
Cell 1	35.9	35.5	35.3	35.2
Cell 2	36.2	35.8	35.6	35.4
Cell 3	36.6	36.2	36.0	35.7
Cell 4	37.0	36.6	36.4	36.1
Cell 5	37.4	36.9	36.7	36.4
Cell 6	37.6	37.2	37.0	36.6
Cell 7	37.8	37.3	37.1	36.7
Cell 8	37.8	37.4	37.2	36.8
Cell 9	37.8	37.4	37.2	36.8
Cell 10	37.7	37.2	37.1	36.7
Cell 11	37.4	37.0	36.8	36.5
Cell 12	37.2	36.8	36.6	36.3

3.1. Effect of cooling insert thickness on module temperatures

The thermal performance of the battery module was analyzed for various cooling insert thicknesses from 0 to 3 mm. 0 mm thickness refers to a condition in which no cooling insert was used in the module. Material properties of aluminium were used to model the cooling insert in this analysis. Average and maximum temperatures of all 12 cell are presented for 4 cooling insert thicknesses in Fig. 2 and Tables 4 and 5.

Steady state calculations were performed under 3C discharge rate and 4 L/min coolant flow rate. In all tested cases, the averaged and maximum temperatures were observed at cell 8 and decreased monotonically outwards towards cells 1 and 12. Recall that cell 1 was near the U-shaped bend in the cooling jacket and cell 12 was near the inlet and outlet of the cooling jacket. The slight skew in the averaged and maximum temperature distribution is driven by the cooling jacket geometry. Cells 1 and 12 also benefits from additional natural convection, but cell 1 temperatures are significant lower since it makes more contact with the U-shaped cooling jacket. Even cells 2 and 3 temperatures are lower than that of cell 12 for the same reason.

Cooling insert thickness also had significant impact on module temperatures. Results presented in Fig. 2 show decreasing averaged and maximum temperatures with thicker cooling inserts likely due to increased heat capacity of the added material.

Table 5
Maximum temperature data from Fig. 2.

	0 mm [°C]	1 mm [°C]	2 mm [°C]	3 mm [°C]
Cell 1	38.6	38.0	37.7	37.4
Cell 2	39.0	38.3	38.0	37.7
Cell 3	39.4	38.8	38.4	38.0
Cell 4	39.8	39.1	38.8	38.4
Cell 5	40.0	39.4	39.1	38.7
Cell 6	40.2	39.6	39.3	38.9
Cell 7	40.2	39.7	39.4	39.0
Cell 8	40.3	39.8	39.5	39.0
Cell 9	40.3	39.7	39.5	39.0
Cell 10	40.2	39.7	39.4	38.9
Cell 11	40.0	39.5	39.2	38.8
Cell 12	39.9	39.3	39.0	38.6

Table 6
Heat flux from the cooling insert to the TIM.

Cooling insert thickness	0 mm	1 mm	2 mm	3 mm
Heat flux from cooling insert [W m^{-2}]		29.47	61.03	93.17
Total heat flux into TIM [W m^{-2}]	444.3	465.8	489.3	514.0

Table 7
Thermal properties of cooling insert materials.

Materials	Plastic	Copper	Aluminium
Thermal conductivity [W m^{-1} K^{-1}]	0.163	398	237
Density [kg m^{-3}]	1070	8930	2700
Specific heat [J kg^{-1} K^{-1}]	1990	385	903

A 3 mm cooling insert reduced the average and maximum temperatures by more than 2 °C across all cells compared to a module without an insert. Maximum temperatures remained below 40 °C for all cells even with a 1 mm cooling insert at a discharge rate of 3C. However, 7 out of 12 cells reported maximum temperatures in excess of 40 °C if no cooling insert was implemented (0 mm). This is due to the cooling insert heat capacity increasing with thickness thereby improving the cooling performance of the module. Furthermore, the cooling insert had a much higher thermal conductivity compared to a battery cell enabling a more efficient cooling.

The cooling insert also prevents direct heat conduction between neighboring battery cells and increases the heat transfer area from the cells to the TIM. Steady state heat flux from a 3 mm cooling insert to the TIM at a discharge rate of 3C ranged from 6 to 10 kW/m^2, where sections that overlap the cooling jacket registered the highest heat flux. Direct heat flux from a battery cell to the TIM range from 4 to 8 kW/m^2, lower than those of the cooling insert.

Heat flux can quickly scale up at higher discharge rates which further increase the need for a cooling insert. Positive heat flux from the cell to the insert can be observed in the upper sections of the insert away from the TIM. Heat transfer from the insert to the TIM in the lower one-fifth of the insert, closer to the TIM but at a much higher rate. Results show that heat generated in most areas of a cell is conducted into the cooling insert. Only a small portion of the battery (near the TIM) conducts heat directly into the TIM. Intense heat conduction between the cooling insert and the TIM was also be observed near their intersections. The total heat flux from the cooling insert to the TIM at thicknesses from 1 to 3 mm are listed in Table 6. Results show a linear increase in heat flux as the cooling insert thickness increases indicating improved cooling performance. A 3 mm cooling insert increased the total heat flux by 70 W/m^2 or 15.6% compared to a module without a cooling insert.

3.2. Effect of cooling insert material on module temperatures

The thermal performance of a battery module was analyzed for various cooling insert materials such as aluminium, copper, and plastic. Material properties of the aforementioned materials are listed in Table 7. Steady state calculations are performed using a 3 mm thick cooling insert, 3C discharge rate and 4 L/min coolant flow rate (see Table 8). Average temperatures of all 12 cell are presented for plastic, aluminium, and copper in Fig. 3.

Overall, the use of any cooling insert produced lower cell temperatures by a minimum of 0.7 °C compared to a module without a cooling insert. Even the plastic cooling insert, despite having a lower thermal conductivity than the battery cell, resulted in lower cell temperatures. Among the three tested material, copper achieved the lowest average cell temperatures across all 12 cells. The aluminium cooling insert performance was very similar to that of copper, with an average cell temperature difference of about 0.15 °C. The plastic cooling insert produced the hottest cell temperatures by up to 0.56 °C compared to copper. Despite significant differences in thermal conductivity between metallic and plastic cooling inserts, temperature differences between the copper and plastic cooling insert was relatively small. This is likely due to plastic having much higher specific heat than aluminium or copper.

Temperature uniformity is also impacted by the cooling insert material. Cells in metallic cooling inserts had a temperature variation of 1.64 °C between the hottest and coldest cells. The variation increased to 1.9 °C for the plastic cooling insert.

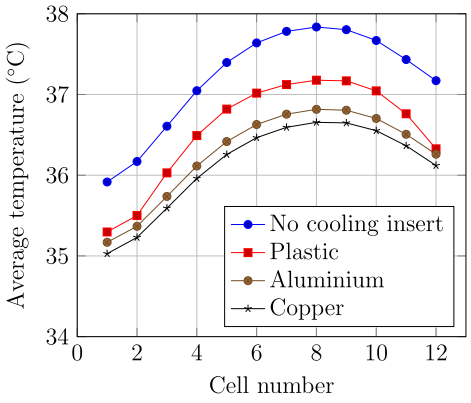

Fig. 3. Average cell temperatures for various cooling insert material.

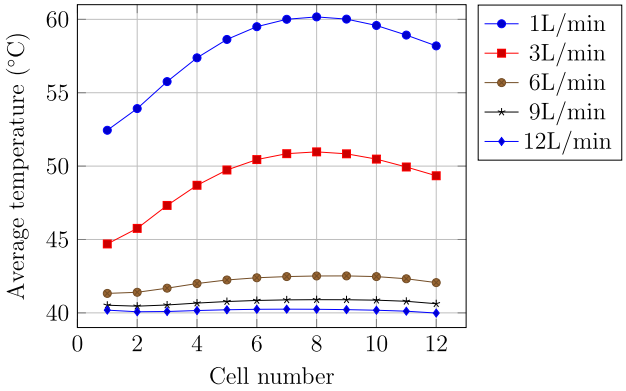

Fig. 4. Average cell temperatures under various coolant flow rates.

Table 8
Temperature data from Fig. 3.

	No insert [°C]	Plastic [°C]	Aluminium [°C]	Copper [°C]
Cell 1	35.9	35.3	35.2	35.0
Cell 2	36.2	35.5	35.4	35.2
Cell 3	36.6	36.0	35.7	35.6
Cell 4	37.0	36.5	36.1	36.0
Cell 5	37.4	36.8	36.4	36.3
Cell 6	37.6	37.0	36.6	36.5
Cell 7	37.8	37.1	36.8	36.6
Cell 8	37.8	37.2	36.8	36.7
Cell 9	37.8	37.2	36.8	36.6
Cell 10	37.7	37.0	36.7	36.6
Cell 11	37.4	36.8	36.5	36.4
Cell 12	37.2	36.2	36.3	36.1

3.3. Effect of flow rate on module temperatures

The thermal performance of a battery module was analyzed for various coolant flow rates from 1 to 12 L/min. Material properties of aluminium was used for the 3 mm cooling insert. Steady state calculations were performed under 4C discharge rate. The coolant pressure drop and the temperature change between the cooling jacket inlet and outlet for all tested flow rates were also assessed.

As expected, results show higher pressure drops and lower temperatures with increasing flow rate due to higher convective heat transfer coefficient. The pressure drop increases monotonically with flow rate from around 62 Pa at 1 L/min to 2570 Pa at 12 L/min. Conversely, the coolant temperature difference between the outlet and the inlet decreases monotonically with increasing flow rate. At the slowest (1 L/min) and fastest (12 L/min) flow rates, the coolant temperature increased by around 10.7 °C and 0.8 °C, respectively. As shown in Fig. 4, flow rates above 8 L/min yielded very small improvements in temperature (less than 1 °C difference) with little to no difference in cooling performance. Significant average cell temperature reduction was observed between

Table 9
Temperature data from Fig. 4.

	1 lpm [°C]	3 lpm [°C]	6 lpm [°C]	9 lpm [°C]	12 lpm [°C]
Cell 1	52.4	44.7	41.3	40.5	40.2
Cell 2	55.8	47.3	41.4	40.5	40.0
Cell 3	53.9	45.8	41.7	40.5	40.1
Cell 4	57.4	48.7	42.0	40.6	40.1
Cell 5	58.6	49.7	42.2	40.7	40.2
Cell 6	59.5	50.4	42.4	40.8	40.2
Cell 7	60.0	50.8	42.5	40.9	40.3
Cell 8	60.2	51.0	42.5	40.9	40.2
Cell 9	60.0	50.8	42.5	40.9	40.2
Cell 10	59.6	50.5	42.5	40.8	40.2
Cell 11	58.9	50.0	42.3	40.8	40.1
Cell 12	58.2	49.3	42.0	40.6	40.0

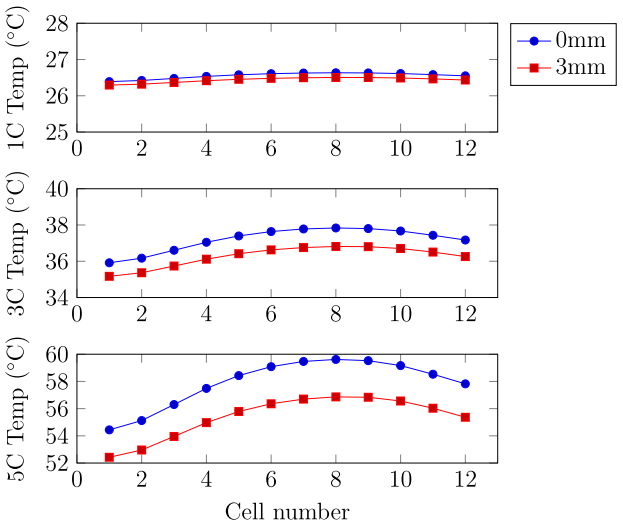

Fig. 5. Average cell temperatures with and without cooling insert under various C-rates.

1 and 6 L/min, from 60.2 °C to 42.5 °C in cell 8. However between 7 L/min and 12 L/min, average cell temperatures were only reduced from 41.7 °C to 40.2 °C in the same cell. Temperature uniformity follows a similar trend where between 1 and 6 L/min, the difference between the hottest and coldest cell was reduced from 7.7 °C to 1.2 °C. Between 7 L/min and 12 L/min, it was reduced from 0.81 °C to 0.27 °C. While higher flow rates reduce average cell temperatures and improve temperature uniformity of the module, its effectiveness quickly diminishes beyond 7 L/min. An optimal coolant flow rate must provide a good balance of pressure drop and cooling performance. For the given condition of 4C discharge rate and 3 mm thick aluminium cooling insert, 7 L/min coolant flow rate was determined to be the most effective overall (see Table 9).

3.4. Effect of C-rates on module temperature

The thermal performance of a battery module was evaluated for discharge rates from 1C to 5C. C-rates affect the heat generation in each battery cell as shown in Fig. 5. Numerical analyses were conducted at steady state, coolant flow rate of 4 L/min, and aluminium cooling insert thicknesses were varied from 0 to 3 mm. For all discharge rates, the average temperature reduction improved with higher cooling insert thickness. The effect was less pronounced at 1C to 2C (less than 0.5 °C), but the differences can exceed 2.5 °C at 5C and 3 mm thick cooling insert. Furthermore, temperature uniformity also decreased with higher discharge rates. Temperature uniformity worsened from 0.24 °C at 1C to 5.2 °C at 5C for modules without a cooling insert. Modules with a 3 mm thick cooling insert performed a bit better, from 0.21 °C at 1C to 4.4 °C at 5C. Significant temperature variations within a battery cell can accelerate capacity fade [60] and must be avoided. However, such temperature variations are unavoidable under the proposed design since cooling only occurs at the bottom of the battery cell.

Overall, the cooling insert design can lower average cell temperatures as well as temperature distribution within the module. It can also maintain cell temperatures to within 40 °C under steady discharge rate of 4C at all tested conditions. While safe temperature limit was exceeded at a steady 5C, high discharge rates in excess of 4C occurs infrequently and temporarily such that even a 3 mm thick cooling plate would be adequate (see Table 10).

Table 10
Temperature data from Fig. 5.

	0 mm, 1C [°C]	0 mm, 3C [°C]	0 mm, 5C [°C]	3 mm, 1C [°C]	3 mm, 3C [°C]	3 mm, 5C [°C]
Cell 1	26.4	35.9	54.4	27.0	35.2	52.4
Cell 2	26.4	36.2	55.1	26.3	35.4	53.0
Cell 3	26.5	36.6	56.3	26.4	35.7	53.9
Cell 4	26.5	37.0	57.4	26.4	36.1	55.0
Cell 5	26.6	37.4	58.4	26.5	36.4	55.8
Cell 6	26.6	37.6	59.0	26.5	36.6	56.4
Cell 7	26.6	37.8	59.5	26.5	36.8	56.7
Cell 8	26.6	37.8	59.6	26.5	36.8	56.9
Cell 9	26.6	37.8	59.5	26.5	36.8	56.8
Cell 10	26.6	37.7	59.2	26.5	36.7	56.6
Cell 11	26.6	37.4	58.5	26.5	36.5	56.0
Cell 12	26.6	37.2	57.8	26.4	36.2	55.4

4. Conclusions

Numerical thermofluidic analyses of a prismatic NCM Li-ion battery module integrated with a cooling insert were performed in this study. Thermal performances of the battery module were evaluated under various conditions such as cooling insert thickness and material, coolant flow rate, and discharge rate. The following conclusions can be drawn from the results.

1. A 3 mm thick cooling insert increased the heat flux into the TIM by up to 15.6% compared to a module without a cooling insert thereby enhancing cooling performance.
2. Various cooling insert materials were analyzed including plastic and two metals (copper and aluminium). Results showed 0.7 and 1.0 °C reduction in temperature for plastic and metallic inserts, respectively, indicating that the presence of a cooling insert can be a significant factor in lowering the module temperatures and improving its temperature uniformity.
3. Higher coolant flow rate significantly improved the cooling performance of the module up to a certain limit. For a discharge rate of 4C, the optimal flow rate was 7 L/min.
4. Higher discharge rate significantly increased the temperature differences within a cell but a 3 mm cooling insert was able to reduce this difference by up to 4 °C thereby improving the performance and durability of the battery module.
5. The results of this study could potentially lead to the development of a compact and low-cost intra-cell heat spreader in a battery module that can be readily implemented in production EVs.

CRediT authorship contribution statement

Jeonggwan Han: Methodology, Data curation, Software, Roles/Writing – original draft. **Wonjin Ko:** Conceptualization, Investigation, Data curation. **Myung-Seop Lim:** Validation, Project administration. **Tonghun Lee:** Writing – review & editing, Resources. **Jihyung Yoo:** Funding acquisition, Writing – review & editing, Supervision.

Declaration of competing interest

The authors declare that they have no known competing financial interests or personal relationships that could have appeared to influence the work reported in this paper.

Data availability

Data will be made available on request.

Acknowledgments

This work was supported by the National Research Foundation of Korea, South Korea (NRF) grant NRF-2020R1A4A4079701 (MSIT), and the Korea Institute for Advancement of Technology, South Korea (KIAT) grant No. P0017120 (MOTIE).

References

[1] M. Muratori, M. Alexander, D. Arent, M. Bazilian, P. Cazzola, E.M. Dede, J. Farrell, C. Gearhart, D. Greene, A. Jenn, et al., The rise of electric vehicles—2020 status and future expectations, Prog. Energy 3 (2) (2021) 022002.

[2] O. Van Vliet, A.S. Brouwer, T. Kuramochi, M. van Den Broek, A. Faaij, Energy use, cost and CO2 emissions of electric cars, J. Power Sources 196 (4) (2011) 2298–2310.

[3] N.C. Onat, M. Kucukvar, O. Tatari, Well-to-wheel water footprints of conventional versus electric vehicles in the United States: A state-based comparative analysis, J. Clean. Prod. 204 (2018) 788–802.

[4] R. Zhao, S. Zhang, J. Liu, J. Gu, A review of thermal performance improving methods of lithium ion battery: Electrode modification and thermal management system, J. Power Sources 299 (2015) 557–577.
[5] J. Cao, G. Hu, Z. Peng, K. Du, Y. Cao, Polypyrrole-coated LiCoO2 nanocomposite with enhanced electrochemical properties at high voltage for lithium-ion batteries, J. Power Sources 281 (2015) 49–55.
[6] J. Deng, C. Bae, J. Marcicki, A. Masias, T. Miller, Safety modelling and testing of lithium-ion batteries in electrified vehicles, Nat. Energy 3 (4) (2018) 261–266.
[7] H. Liu, Z. Wei, W. He, J. Zhao, Thermal issues about Li-ion batteries and recent progress in battery thermal management systems: A review, Energy Convers. Manage. 150 (2017) 304–330.
[8] D.H. Jeon, S.M. Baek, Thermal modeling of cylindrical lithium ion battery during discharge cycle, Energy Convers. Manage. 52 (8–9) (2011) 2973–2981.
[9] Y. Abdul-Quadir, T. Laurila, J. Karppinen, K. Jalkanen, K. Vuorilehto, L. Skogström, M. Paulasto-Kröckel, Heat generation in high power prismatic Li-ion battery cell with LiMnNiCoO2 cathode material, Int. J. Energy Res. 38 (11) (2014) 1424–1437.
[10] J. Jaguemont, L. Boulon, Y. Dubé, A comprehensive review of lithium-ion batteries used in hybrid and electric vehicles at cold temperatures, Appl. Energy 164 (2016) 99–114.
[11] X. Feng, M. Ouyang, X. Liu, L. Lu, Y. Xia, X. He, Thermal runaway mechanism of lithium ion battery for electric vehicles: A review, Energy Storage Mater. 10 (2018) 246–267.
[12] Y. Li, H. Guo, F. Qi, Z. Guo, M. Li, Comparative study of the influence of open circuit voltage tests on state of charge online estimation for lithium-ion batteries, IEEE Access 8 (2020) 17535–17547.
[13] Y. Zou, X. Hu, H. Ma, S.E. Li, Combined state of charge and state of health estimation over lithium-ion battery cell cycle lifespan for electric vehicles, J. Power Sources 273 (2015) 793–803.
[14] S. Yalçın, S. Panchal, M.S. Herdem, A CNN-ABC model for estimation and optimization of heat generation rate and voltage distributions of lithium-ion batteries for electric vehicles, Int. J. Heat Mass Transfer 199 (2022) 123486.
[15] H. Najafi Khaboshan, F. Jaliliantabar, A.A. Abdullah, S. Panchal, Improving the cooling performance of cylindrical lithium-ion battery using three passive methods in a battery thermal management system, 2022, Available At SSRN 4276692.
[16] A. Mevawalla, Y. Shabeer, M.K. Tran, S. Panchal, M. Fowler, R. Fraser, Thermal modelling utilizing multiple experimentally measurable parameters, Batteries 8 (10) (2022) 147.
[17] Y. Xie, Y. Liu, M. Fowler, M.-K. Tran, S. Panchal, W. Li, Y. Zhang, Enhanced optimization algorithm for the structural design of an air-cooled battery pack considering battery lifespan and consistency, Int. J. Energy Res. (2022).
[18] Y. Xie, W. Li, X. Hu, M.-K. Tran, S. Panchal, M. Fowler, K. Liu, Co-estimation of SOC and three-dimensional SOT for lithium-ion batteries based on distributed spatial-temporal online correction, IEEE Trans. Ind. Electron. (2022).
[19] Y. Xu, H. Zhang, X. Xu, X. Wang, Numerical analysis and surrogate model optimization of air-cooled battery modules using double-layer heat spreading plates, Int. J. Heat Mass Transfer 176 (2021) 121380.
[20] Y. Wang, Y. Yu, Z. Jing, C. Wang, G. Zhou, W. Zhao, Thermal performance of lithium-ion batteries applying forced air cooling with an improved aluminium foam heat sink design, Int. J. Heat Mass Transfer 167 (2021) 120827.
[21] W. Yang, F. Zhou, H. Zhou, Y. Liu, Thermal performance of axial air cooling system with bionic surface structure for cylindrical lithium-ion battery module, Int. J. Heat Mass Transfer 161 (2020) 120307.
[22] S. Panchal, I. Dincer, M. Agelin-Chaab, R. Fraser, M. Fowler, Experimental temperature distributions in a prismatic lithium-ion battery at varying conditions, Int. Commun. Heat Mass Transfer 71 (2016) 35–43.
[23] S. Panchal, R. Khasow, I. Dincer, M. Agelin-Chaab, R. Fraser, M. Fowler, Numerical modeling and experimental investigation of a prismatic battery subjected to water cooling, Numer. Heat Transf. Part A: Appl. 71 (6) (2017) 626–637.
[24] Z. Shang, H. Qi, X. Liu, C. Ouyang, Y. Wang, Structural optimization of lithium-ion battery for improving thermal performance based on a liquid cooling system, Int. J. Heat Mass Transfer 130 (2019) 33–41.
[25] Z. Sun, R. Fan, F. Yan, T. Zhou, N. Zheng, Thermal management of the lithium-ion battery by the composite PCM-Fin structures, Int. J. Heat Mass Transfer 145 (2019) 118739.
[26] D. Zou, X. Ma, X. Liu, P. Zheng, Y. Hu, Thermal performance enhancement of composite phase change materials (PCM) using graphene and carbon nanotubes as additives for the potential application in lithium-ion power battery, Int. J. Heat Mass Transfer 120 (2018) 33–41.
[27] T. Wang, K. Tseng, J. Zhao, Z. Wei, Thermal investigation of lithium-ion battery module with different cell arrangement structures and forced air-cooling strategies, Appl. Energy 134 (2014) 229–238.
[28] R. Mahamud, C. Park, Reciprocating air flow for Li-ion battery thermal management to improve temperature uniformity, J. Power Sources 196 (13) (2011) 5685–5696.
[29] L.H. Saw, Y. Ye, A.A. Tay, W.T. Chong, S.H. Kuan, M.C. Yew, Computational fluid dynamic and thermal analysis of lithium-ion battery pack with air cooling, Appl. Energy 177 (2016) 783–792.
[30] D. Chalise, K. Shah, R. Prasher, A. Jain, Conjugate heat transfer analysis of thermal management of a Li-ion battery pack, J. Electrochem. Energy Convers. Storage 15 (1) (2018).
[31] Y. Huo, Z. Rao, X. Liu, J. Zhao, Investigation of power battery thermal management by using mini-channel cold plate, Energy Convers. Manage. 89 (2015) 387–395.
[32] S. Panchal, R. Khasow, I. Dincer, M. Agelin-Chaab, R. Fraser, M. Fowler, Thermal design and simulation of mini-channel cold plate for water cooled large sized prismatic lithium-ion battery, Appl. Therm. Eng. 122 (2017) 80–90.
[33] L. Jin, P. Lee, X. Kong, Y. Fan, S. Chou, Ultra-thin minichannel LCP for EV battery thermal management, Appl. Energy 113 (2014) 1786–1794.
[34] A. Jarrett, I.Y. Kim, Design optimization of electric vehicle battery cooling plates for thermal performance, J. Power Sources 196 (23) (2011) 10359–10368.
[35] X.-H. Yang, S.-C. Tan, J. Liu, Thermal management of Li-ion battery with liquid metal, Energy Convers. Manage. 117 (2016) 577–585.
[36] A.M. Sefidan, A. Sojoudi, S.C. Saha, Nanofluid-based cooling of cylindrical lithium-ion battery packs employing forced air flow, Int. J. Therm. Sci. 117 (2017) 44–58.
[37] B. Mondal, C.F. Lopez, P.P. Mukherjee, Exploring the efficacy of nanofluids for lithium-ion battery thermal management, Int. J. Heat Mass Transfer 112 (2017) 779–794.
[38] M.W. Nazir, M. Nazeer, T. Javed, N. Ali, K. Al-Basyouni, M.I. Khan, Hydrothermal features of the magnetite nanoparticles on natural convection flow through a square conduit by using the finite element method, Internat. J. Modern Phys. B (2022) 2350069.
[39] M. Irfan, M. Nazeer, F. Hussain, I. Siddique, Heat transfer analysis in the peristaltic flow of casson nanofluid through asymmetric channel with velocity and thermal slips: Applications in a complex system, Internat. J. Modern Phys. B 36 (32) (2022) 2250231.
[40] M.W. Nazir, T. Javed, N. Ali, M. Nazeer, M.I. Khan, Theoretical investigation of thermal analysis in aluminum and titanium alloys filled in nanofluid through a square cavity having the uniform thermal condition, Internat. J. Modern Phys. B 36 (22) (2022) 2250140.
[41] A. Al-Zubaidi, M. Nazeer, K. Khalid, S. Yaseen, S. Saleem, F. Hussain, Thermal analysis of blood flow of Newtonian, pseudo-plastic, and dilatant fluids through an inclined wavy channel due to metachronal wave of cilia, Adv. Mech. Eng. 13 (9) (2021) 16878140211049060.
[42] N. Ali, M. Nazeer, T. Javed, M. Razzaq, Finite element analysis of bi-viscosity fluid enclosed in a triangular cavity under thermal and magnetic effects, Eur. Phys. J. Plus 134 (1) (2019) 1–20.

[43] M. Nazeer, Development and theoretical analysis of slippery walls flow of third-grade fluid through the convergent symmetric channel, Waves Random Complex Media (2022) 1–20.
[44] Y. Zheng, Y. Shi, Y. Huang, Optimisation with adiabatic interlayers for liquid-dominated cooling system on fast charging battery packs, Appl. Therm. Eng. 147 (2019) 636–646.
[45] K.S. Kshetrimayum, Y.-G. Yoon, H.-R. Gye, C.-J. Lee, Preventing heat propagation and thermal runaway in electric vehicle battery modules using integrated PCM and micro-channel plate cooling system, Appl. Therm. Eng. 159 (2019) 113797.
[46] F. Chen, R. Huang, C. Wang, X. Yu, H. Liu, Q. Wu, K. Qian, R. Bhagat, Air and PCM cooling for battery thermal management considering battery cycle life, Appl. Therm. Eng. 173 (2020) 115154.
[47] Z. Wang, Z. Zhang, L. Jia, L. Yang, Paraffin and paraffin/aluminum foam composite phase change material heat storage experimental study based on thermal management of Li-ion battery, Appl. Therm. Eng. 78 (2015) 428–436.
[48] Z. Ling, F. Wang, X. Fang, X. Gao, Z. Zhang, A hybrid thermal management system for lithium ion batteries combining phase change materials with forced-air cooling, Appl. Energy 148 (2015) 403–409.
[49] R. Sabbah, R. Kizilel, J. Selman, S. Al-Hallaj, Active (air-cooled) vs. passive (phase change material) thermal management of high power lithium-ion packs: Limitation of temperature rise and uniformity of temperature distribution, J. Power Sources 182 (2) (2008) 630–638.
[50] L. Wang, Y. Cheng, X. Zhao, A LiFePO4 battery pack capacity estimation approach considering in-parallel cell safety in electric vehicles, Appl. Energy 142 (2015) 293–302.
[51] X. Yang, X. Gao, F. Zhang, W. Luo, Y. Duan, Experimental study on temperature difference between the interior and surface of $Li[Ni_{1/3}Co_{1/3}Mn_{1/3}]O_2$ prismatic lithium-ion batteries at natural convection and adiabatic condition, Appl. Therm. Eng. 190 (2021) 116746.
[52] M.J. Moran, H.N. Shapiro, D.D. Boettner, M.B. Bailey, Fundamentals of engineering thermodynamics, John Wiley & Sons, 2010.
[53] V.V. Viswanathan, D. Choi, D. Wang, W. Xu, S. Towne, R.E. Williford, J.-G. Zhang, J. Liu, Z. Yang, Effect of entropy change of lithium intercalation in cathodes and anodes on Li-ion battery thermal management, J. Power Sources 195 (11) (2010) 3720–3729.
[54] H.K. Versteeg, W. Malalasekera, An Introduction to Computational Fluid Dynamics: The Finite Volume Method, Pearson education, 2007.
[55] G. Bangga, T. Kusumadewi, G. Hutomo, A. Sabila, T. Syawitri, H. Setiadi, M. Faisal, R. Wiranegara, Y. Hendranata, D. Lastomo, et al., Improving a two-equation eddy-viscosity turbulence model to predict the aerodynamic performance of thick wind turbine airfoils, J. Phys. Conf. Ser. 974 (2018) 012019.
[56] F. Moukalled, L. Mangani, M. Darwish, The finite volume method, in: The Finite Volume Method in Computational Fluid Dynamics, Springer, 2016, pp. 103–135.
[57] H. Jasak, A. Jemcov, Z. Tukovic, et al., OpenFOAM: A C++ library for complex physics simulations, in: International Workshop on Coupled Methods in Numerical Dynamics, Vol. 1000, IUC Dubrovnik Croatia, 2007, pp. 1–20.
[58] M. Nazeer, A. Al-Zubaidi, F. Hussain, F.Z. Duraihem, S. Anila, S. Saleem, Thermal transport of two-phase physiological flow of non-Newtonian fluid through an inclined channel with flexible walls, Case Stud. Therm. Eng. (2022) 102146.
[59] F. Hussain, M. Nazeer, M. Altanji, A. Saleem, M. Ghafar, Thermal analysis of Casson rheological fluid with gold nanoparticles under the impact of gravitational and magnetic forces, Case Stud. Therm. Eng. 28 (2021) 101433.
[60] Y. Kim, S. Mohan, J.B. Siegel, A.G. Stefanopoulou, Y. Ding, The estimation of temperature distribution in cylindrical battery cells under unknown cooling conditions, IEEE Trans. Control Syst. Technol. 22 (6) (2014) 2277–2286.